Laser Photonics Rev. **7**, No. 2, 171–187 (2013) / **DOI** 10.1002/lpor.201200003

LASER & PHOTONICS REVIEWS

Abstract Recent years have seen a growing interest in using metal nanostructures to control temperature on the nanoscale. Under illumination at its plasmonic resonance, a metal nanoparticle features enhanced light absorption, turning it into an ideal nano-source of heat, remotely controllable using light. Such a powerful and flexible photothermal scheme is the basis of *thermo-plasmonics*. Here, the recent progress of this emerging and fast-growing field is reviewed. First, the physics of heat generation in metal nanoparticles is described, under both continuous and pulsed illumination. The second part is dedicated to numerical and experimental methods that have been developed to further understand and engineer plasmonic-assisted heating processes on the nanoscale. Finally, some of the most recent applications based on the heat generated by gold nanoparticles are surveyed, namely photothermal cancer therapy, nanosurgery, drug delivery, photothermal imaging, protein tracking, photoacoustic imaging, nano-chemistry and optofluidics.

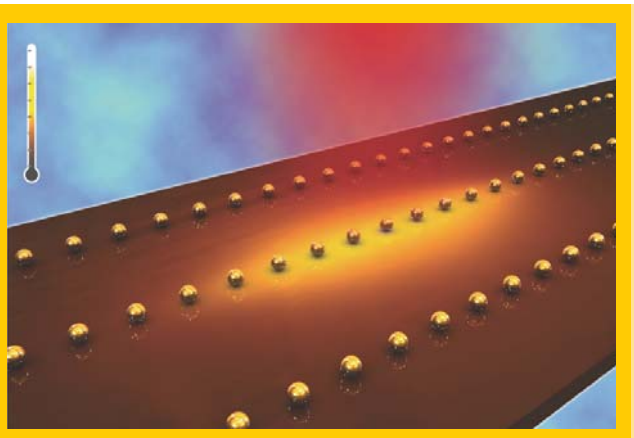

REVIEW ARTICLE

Thermo-plasmonics: using metallic nanostructures as nano-sources of heat

Guillaume Baffou[1,*] **and Romain Quidant**[2,3,*]

1. Introduction

Noble metal nanoparticles (NPs) have received over the last decade much interest in nanoscience due to their remarkable optical properties [1]. In particular, gold NPs feature resonances that can be tuned from the visible to the infrared frequency ranges. These resonances, known as localized surface plasmons (LSPs), are responsible for both enhanced light scattering and enhanced light absorption. For a long time, the absorption and the subsequent NP temperature increase have been considered as side effects in plasmonics applications, which focused on the optical properties of metal NPs. Only recently have scientists realized that this enhanced light absorption, turning metal NPs into ideal nano-sources of heat remotely controllable using light, provides an unprecedented way to control thermal-induced phenomena at the nanoscale [2].

In this article, we review the recent progress in the emerging and fast-growing field of thermo-plasmonics, which investigates the use of plasmonic structures as nano-sources of heat. We first describe the physics of heat generation in metal NPs. In particular, we emphasize the differences in the heating mechanisms between continuous and pulsed illuminations. Then, we present the numerical frameworks that have been developed to model the photothermal properties of metal NPs. We also discuss recent experimental works that aim at addressing the intricate problem of probing and imaging the temperature distribution generated around plasmonic nanostructures. Finally, we review the main emerging applications in thermo-plasmonics, from medical therapy and bio-imaging to nano-chemistry and optofluidics.

2. Physics of plasmonic heating

In this section, we consider a metal NP of complex relative permittivity $\varepsilon(\omega)$ immersed in a dielectric surrounding medium of real relative permittivity $\varepsilon_s = n_s^2$. This NP is illuminated by monochromatic light at an angular frequency ω with $\mathbf{E}_0(\mathbf{r};\omega)$ the complex amplitude of the incident electric field. (For any physical quantity $A(\mathbf{r},t)$, we define its complex amplitude $A(\mathbf{r})$ such that $A(\mathbf{r},t) = \mathrm{Re}[A(\mathbf{r})\,e^{i\omega t}]$.) We define $\omega = k_0 c_0 = 2\pi c_0/\lambda_0 = 2\pi c_0/n_s\lambda = c_0 k/n_s$, where c_0 is the speed of light, λ_0 the free-space wavelength, λ the wavelength in the surrounding medium, and k_0 and k the angular wave number in free space and in the medium, respectively.

2.1. Metallic nanoparticles and localized surface plasmons

Metal nano-objects support electronic resonances known as LSPs that can be excited upon illumination. The frequency

[1] Institut Fresnel, CNRS, Aix-Marseille Université, Domaine Universitaire Saint-Jérôme, 13397 Marseille, France [2] ICFO – Institut de Ciencies Fotoniques, Mediterranean Technology Park, 08860 Castelldefels, Barcelona, Spain [3] ICREA – Institució Catalana de Recerca i Estudis Avançats, 08010 Barcelona, Spain
[*] Corresponding authors: e-mail: guillaume.baffou@fresnel.fr, romain.quidant@icfo.es

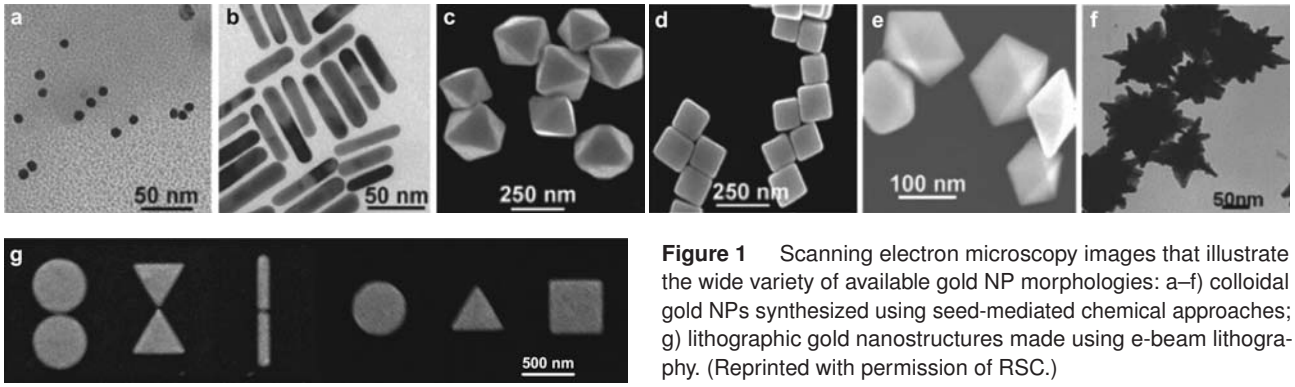

Figure 1 Scanning electron microscopy images that illustrate the wide variety of available gold NP morphologies: a–f) colloidal gold NPs synthesized using seed-mediated chemical approaches; g) lithographic gold nanostructures made using e-beam lithography. (Reprinted with permission of RSC.)

of LSP resonances strongly depends on the morphology of the metal nano-object and its dielectric environment. For instance, elongating a sphere into a rod-like shape tends to red-shift the LSP resonance. For noble metals, such as gold, silver or copper, this property allows accurate tuning of LSP resonances from the visible to the near-infrared (NIR) frequency range.

Recent advances in both *bottom-up* and *top-down* fabrication techniques offer a tremendous variety of metal NP sizes and shapes. On the one hand, chemists have developed synthesis procedures to produce colloidal noble metal NPs with numerous geometries including rods, cubes, triangles, shells, stars, etc. [3]. On the other hand, techniques such as e-beam lithography and focused ion beam milling are convenient means to design planar metal nanostructures on a flat substrate with a resolution down to a few tens of nanometers. Examples of colloidal gold NPs and lithographically prepared gold nanostructures are presented in Fig. 1.

The origin of LSP resonances in metal NPs can be simply derived for a metal sphere that is much smaller than the illumination wavelength and can be considered as an electromagnetic dipole. In this case, the sphere polarizability reads

$$\alpha(\omega) = 4\pi R^3 \frac{\varepsilon(\omega) - \varepsilon_s}{\varepsilon(\omega) + 2\varepsilon_s}. \tag{1}$$

where R is th radius of the sphere. In this expression, the polarizability α is defined such that the complex amplitude of the polarization vector of the NP reads $\mathbf{P} = \varepsilon_0 \varepsilon_s \alpha \mathbf{E}_0$. Equation (1) shows that a resonance occurs at the frequency ω at which $\varepsilon(\omega) \approx -2\varepsilon_s$. For a gold sphere smaller than ~ 30 nm in water, this occurs for $\lambda \approx 530$ nm. However, for larger spheres, this dipolar approximation is no longer valid and more complex models, such as Mie theory [4–6], accounting for retardation effects, are required. For more sophisticated geometries, numerical simulations are needed (see Section 3.1).

Such a resonance in the polarizability is responsible for a resonance both in absorption and scattering. For any NP morphology, the efficiency of these processes can be described by absorption and scattering cross-sections [4, 5]:

$$\sigma_{abs} = k\,\mathrm{Im}(\alpha) - \frac{k^4}{6\pi}|\alpha|^2, \tag{2}$$

$$\sigma_{scat} = \frac{k^4}{6\pi}|\alpha|^2, \tag{3}$$

$$\sigma_{ext} = \sigma_{abs} + \sigma_{scat} = k\,\mathrm{Im}(\alpha). \tag{4}$$

The relative efficiency of absorption and scattering processes can be quantified by the photothermal efficiency $\mu = \sigma_{abs}/\sigma_{ext}$, which depends mostly on the NP morphology [7, 8]. For instance, for spherical gold NPs smaller than 90 nm (in water), absorption is dominant ($\mu \approx 1$), while for bigger gold NPs, scattering dominates ($\mu < 1$), as shown in Fig. 2a. Note that this conclusion is valid when considering the *respective maxima* of both cross-section spectra, but not the cross-sections at an arbitrary wavelength. Indeed, as shown in Fig. 2b, for an 88 nm NP, even though the respective maxima of the absorption and scattering spectra are equal, absorption can be either dominant or negligible depending on the wavelength. This is the consequence of the spectral shift that usually occurs between absorption and scattering spectra for large or non-spherical NPs.

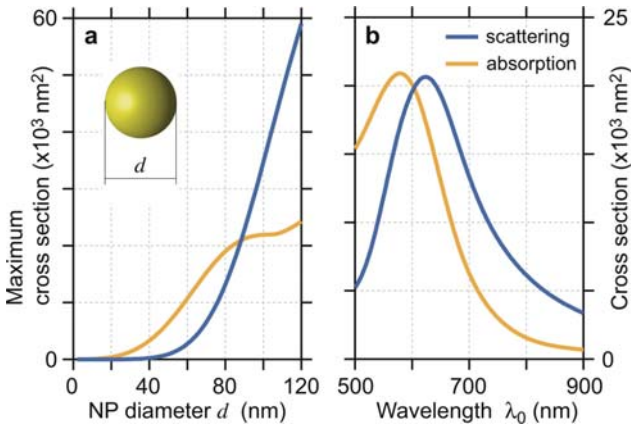

Figure 2 (online color at: www.lpr-journal.org) a) Evolution of the maximum absorption and scattering for increasing diameters of gold NPs. It is shown that spherical gold NPs smaller than 90 nm are more efficient absorbers than scatterers. b) Absorption and scattering cross-section spectra for a gold nanosphere in water, 88 nm in diameter. For this precise diameter, the absorption and scattering maxima are equal. However, due to the spectral shift, absorption can be either dominant or negligible depending on the considered wavelength.

Consequently, even though spherical gold NPs are usually better absorbers than scatterers, the illumination wavelength must be specified to determine what is the actual dominant energy conversion pathway. It is worth noticing that, for this reason, considering experimental *extinction* spectra to estimate the *absorption* efficiency of a plasmonic structure, as sometimes seen in the literature [9], is not always reliable.

Tuning the plasmonic resonance frequency of a NP can be easily achieved by changing its morphology. Any deviation from the spherical shape tends to red-shift the resonance. Experimental results presented in Fig. 3 illustrate the red-shift of the plasmon resonance of a gold nanorod while increasing its aspect ratio.

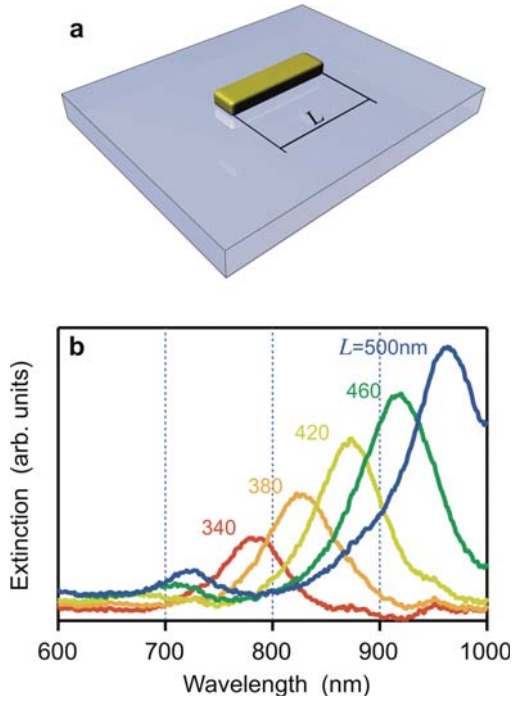

Figure 3 (online color at: www.lpr-journal.org) Experimental extinction spectra measured on matrices of lithographic gold nanorods of increasing lengths L, 40 nm thick and 60 nm wide, lying on a glass substrate.

In the following, we focus on the *absorption* processes and the subsequent heat generation.

2.2. Delivered heat power

The power absorbed (and delivered) by a NP can be simply expressed using the absorption cross-section σ_{abs} introduced in the previous section:

$$Q = \sigma_{\text{abs}} I \tag{5}$$

were I is the irradiance of the incoming light (power per unit surface). In the case of a plane wave, $I = n_s c_0 \varepsilon_0 |\mathbf{E}_0|^2/2$.

The heat generation can be also derived from the heat power density $q(\mathbf{r})$ inside the NP such that $Q = \int_V q(\mathbf{r}) \mathrm{d}^3 r$, where the integral runs over the NP volume V. Since the heat originates from Joule effects, the heat power density reads [10, 11]

$$q(\mathbf{r}) = \frac{1}{2}\mathrm{Re}[\mathbf{J}^\star(\mathbf{r}) \cdot \mathbf{E}(\mathbf{r})] \tag{6}$$

where $\mathbf{J}(\mathbf{r})$ is the complex amplitude of the electronic current density inside the NP. As $\mathbf{J}(\mathbf{r}) = i\omega\mathbf{P}$ and $\mathbf{P} = \varepsilon_0 \varepsilon(\omega)\mathbf{E}$, one ends up with

$$q(\mathbf{r}) = \frac{\omega}{2}\mathrm{Im}(\varepsilon(\omega))\varepsilon_0 |\mathbf{E}(\mathbf{r})|^2 . \tag{7}$$

The heat generation is thus directly proportional to the square of the electric field inside the metal. This is an important aspect to consider when designing efficient plasmonic nano-sources of heat.

In practice there are thus two ways of calculating the heat power Q delivered by a given NP. For geometries for which the absorption cross-section is known (for example for spherical NPs using Eqs. (1) and (2)), Q can be estimated using Eq. (5). However, for more complicated morphologies for which there is no simple analytical expression available, the computation of the inner electric field amplitude $\mathbf{E}(\mathbf{r})$ is required to calculate $q(\mathbf{r})$ from Eq. (7). An example of such a computation is presented in Fig. 4. A gold nanorod with a resonance frequency around $\lambda_0 = 760$ nm is illuminated with a plane wave linearly polarized along its long axis. Interestingly, at resonance, most of the heat originates from the center of the rod rather than from its extremities (Fig. 4b). This can be understood by the fact that the electronic current responsible for the Joule effect mostly flows in the center of the nanorod while the extremities mainly accumulate charges [12].

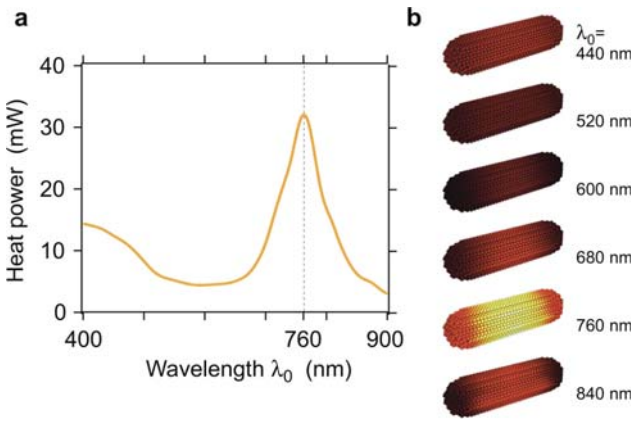

Figure 4 (online color at: www.lpr-journal.org) a) Heat power delivered by a single gold nanorod (50 × 12 nm) as a function of the illumination wavelength calculated using Green's dyadic tensor technique. b) Representation of the heat power density within the nanorod for different illumination wavelengths.

2.3. Temperature profile under continuous-wave illumination

While the computation of the delivered heat power Q turns out to be a full-optical problem as explained in the previous section, the determination of the steady-state temperature distribution $T(\mathbf{r})$ inside and outside the NP is based on the resolution of the heat diffusion equation:

$$\nabla \cdot [\kappa(\mathbf{r}) \nabla T(\mathbf{r})] = -q(\mathbf{r}) \quad \text{inside the NP}, \tag{8}$$

$$\nabla \cdot [\kappa(\mathbf{r}) \nabla T(\mathbf{r})] = 0 \quad \text{outside the NP} \tag{9}$$

where $\kappa(\mathbf{r})$ is the thermal conductivity. For a spherical NP of radius R, simple calculations lead to a temperature increase [13]:

$$\delta T(r) = \delta T_{\mathrm{NP}} \frac{R}{r}, \quad r > R, \tag{10}$$

$$\delta T(r) \approx \delta T_{\mathrm{NP}}, \quad r < R \tag{11}$$

where δT_{NP} is the temperature increase of the NP. Interestingly, while the heat power density $q(\mathbf{r})$ can be highly non-uniform within the NP as clearly observed in Fig. 4 [12], the temperature at equilibrium is, on the contrary, generally perfectly uniform inside the NP [13]. This is due to the much larger thermal conductivity of metals as compared with that of the surroundings (liquid, glass, etc.). The actual temperature increase experienced by a NP is dependent on numerous parameters, namely its absorption cross-section, its shape, the thermal conductivity of the surrounding medium and the wavelength and irradiance of the incoming light. For a spherical NP, the NP temperature increase is related to the absorbed power $Q = \sigma_{\mathrm{abs}} I$ according to [13]

$$\delta T_{\mathrm{NP}} = \frac{Q}{4\pi\kappa_{\mathrm{s}} R} \tag{12}$$

where κ_{s} is the thermal conductivity of the surrounding medium.

To give an order of magnitude, a spherical gold NP in water, 20 nm in diameter, illuminated at $\lambda_0 = 530$ nm with an irradiance of $I = 1\ \mathrm{mW/\mu m^2}$ experiences a temperature increase of ~ 5 °C. Importantly, this simple model may no longer be valid when several NPs are in close proximity as thermal collective effects can occur [14, 15]. In this case, reduced irradiance can be used to achieve the same temperature increase.

The establishment of this steady-state temperature profile is usually very fast when working with NPs. The typical duration τ_{tr} of the transient regime is not dependent on the temperature increase but on the characteristic size L of the system (for instance the radius R for a sphere) [6]:

$$\tau_{\mathrm{tr}} \sim L^2 \frac{\rho c_{\mathrm{p}}}{3\kappa_{\mathrm{s}}} \tag{13}$$

where ρ is the mass density of the NP and c_{p} its specific heat capacity at constant pressure. For example, for spherical NPs of diameters 10 nm, 100 nm and 1 µm, one gets τ_{tr} of the order of 0.1 ns, 10 ns and 1 µs, respectively.

For non-spherical NPs, there is no simple analytical expression giving the NP temperature increase δT_{NP} as a function of the absorbed heat power Q and numerical simulations are required. However, Baffou et al. [13] have recently proposed to use a dimensionless geometrical correction factor β defined such that the NP temperature increase reads

$$\delta T_{\mathrm{NP}} = \frac{Q}{\beta\, 4\pi\kappa_{\mathrm{s}} R_{\mathrm{eq}}} \tag{14}$$

where R_{eq} is the equivalent NP radius. The value of beta for a large set of geometries with axial symmetry (namely rods, ellipsoids, discs and tori) are given in Ref. [13].

Another simple approach developed by the same group [15,16] consists of using what was coined the *Laplace radius* R_{L} of the particle such that the temperature increase simply reads

$$\delta T_{\mathrm{NP}} = \frac{Q}{4\pi\kappa_{\mathrm{s}} R_{\mathrm{L}}}. \tag{15}$$

It was shown that this Laplace radius can be calculated by meshing the NP with a regular lattice containing N points and using the following procedure:

$$R_{\mathrm{L}} = \sum_{i=1}^{N} \sum_{j=1}^{N} (\mathbb{A})^{-1}_{ij} \tag{16}$$

where the $N \times N$ matrix $\mathbb{A}$ is defined such that

$$\mathbb{A}_{ij} = \frac{1}{|\mathbf{r}_i - \mathbf{r}_j|} \quad \text{for } i \neq j, \tag{17}$$

$$\mathbb{A}_{ii} = 2/a \tag{18}$$

where $\mathbf{r}_i$ is the position of the meshing point i and a the lattice constant.

A last feature that is worth discussing is the possible influence of the surface thermal resistivity at the surface of a NP immersed in a liquid [17–20]. A thermal resistivity may occur because of the material discontinuity, which acts as a thermal impedance. This resistivity can play a significant role in the heat release since it can reach appreciable values when the liquid does not wet the solid. The wetting depends on the nature of the interface and, in particular, on a possible molecular coating. Namely, hydrophobic coatings are associated with poor thermal conductivities. The direct consequence of a finite interface conductivity G (or resistivity $1/G$) is a temperature discontinuity δT at the NP interface such that

$$Q = 4\pi R^2 G \delta T. \tag{19}$$

However, in the steady-state regime, this surface resistivity has no effect on the temperature *outside* the NP, in the surrounding medium. As evidenced in Eq. (10), the temperature outside the medium is only dependent on the heat power Q released by the NP. A finite surface conductivity G has only an effect on the temperature within the NP. It can also contribute in making any transient regime longer. The incidence of such a resistivity can be quantified using the Kapitza number λ_{K} defined such that

$$\lambda_{\mathrm{K}} = \frac{\kappa_{\mathrm{s}}}{GR}. \tag{20}$$

The surface resistivity $1/G$ can be neglected in any thermal process if $\lambda_K \ll 1$. For gold NPs in water, usual values of the interface conductivity G range from 50 MW/(m^{2}K) to ∞ [17, 20]. For NP radii ranging from 5 to 50 nm, typical Kapitza numbers λ_K thus range from 2 to ~ 0. As an example, gold nanorods coated with cetyltrimethylammonium bromide (CTAB) molecules are endowed with a typical surface conductivity of $G = 130$ MW/(m^{2}K) [17]. If the nanorods are, say, 50×12 nm in size, the effective radius is $R_{\text{eff}} = 11$ nm and Eq. (20) yields $\lambda_K \approx 0.4$. Hence, in this case, the surface resistivity does not have any significant effect.

2.4. Nanoparticle heating under pulsed illumination

The use of pulsed illumination (from the femtosecond to the nanosecond range) to heat metal NPs markedly increases the range of applications of noble metal NPs. Compared to continuous-wave (CW) illumination, a new class of effects can be triggered, such as shorter temperature and pressure variations [21–23], further temperature confinement [6], acoustic wave generation [22], vibration modes [24–26], bubble formation [27–31], NP shape modification [32–35] and melting [32, 36, 37] and extreme thermodynamics conditions [38–42]. In this section, we briefly discuss the thermodynamics of metal NPs under pulsed illumination and in particular the influence of parameters such as pulse duration, pulsation rate and size of the NP.

The absorption of laser pulse energy by a gold NP can be described as a three-step process [43, 44], each of these steps involving different time scales as follows.

Step 1. Electronic absorption: During the interaction with the laser pulse, part of the incident pulse energy is absorbed by the gas of free electrons of the NP, much lighter and reactive than the ion lattice. The electronic gas thermalizes very fast to a Fermi–Dirac distribution over a time scale $\tau_e \sim 100$ fs [44]. This leads to a state of non-equilibrium within the NP: the electronic temperature T_e of the electronic gas increases while the temperature of the lattice (phonons) T_p remains unchanged.

Step 2. Electron–phonon thermalization: Subsequently, this hot electronic gas relaxes (cools down), through internal electron–phonon interaction characterized by a time scale τ_{e-ph} to thermalize with the ions of the gold lattice. This time scale is not dependent on the size of the NP except for NPs smaller than 5 nm due to confinement effects [45]. Above this size and for moderate pulse energy, the time scale is constant and equals $\tau_{e-ph} \sim 1.7$ ps [46–48]. At this point, the NP is in internal equilibrium at a uniform temperature ($T_e = T_p$), but is not in equilibrium with the surrounding medium that is still at the initial ambient temperature.

Step 3. External heat diffusion: The energy diffusion from the NP to the surroundings usually occurs at longer characteristic time scale τ_{tr} (see Eq. (13)) and leads to a cooling of the NP and a heating of the surrounding medium. The time scale of this process depends on the size of the NP and ranges from 100 ps to a few nanoseconds. For small NPs (< 20 nm), this third step can overlap in time with the electron–phonon thermalization [23] (as discussed hereafter).

During this process, the total absorbed energy $\mathscr{E}_0$ reads

$$\mathscr{E}_0 = \sigma_{abs} \langle I \rangle / f = \sigma_{abs} F \tag{21}$$

where f is the pulsation rate and F the fluence of the laser pulse (energy per unit area).

Different regimes can be observed depending on the pulse duration compared with τ_{tr} (see Eq. (13)). When the pulse duration is short enough (typically < 0.1 ns) and/or the NP is small enough (typically < 100 nm in diameter), the three steps can be considered to happen *successively*. In this regime, the initial temperature increase reaches its maximal value [6]:

$$\delta T^0_{NP} = \frac{\sigma_{abs} F}{V \rho_{Au} c_{Au}} \tag{22}$$

where V is the volume of the NP. (The expression is only valid for moderate temperature increase so that c_{Au} remains constant.) In this case, the duration of the heating of the medium is of the order of τ_{tr}.

If we consider now the regime were the pulse duration exceeds τ_{tr}, the three steps will overlap in time. In other words, heat gets absorbed and delivered in the surroundings simultaneously. In this case, the maximum temperature increase inside the NP will not reach δT^0_{NP} and the heating duration will simply equal the pulse duration. This situation is usually obtained when using *nanosecond* pulses on gold NPs.

Another important aspect to discuss is the spatial extension of the temperature distribution in the surroundings (Fig. 5). While the temperature profile varies as $1/r$ under CW illumination (see Eq. (10)), pulsed illumination makes it possible to further confine the temperature increase at the vicinity of the NP. For example, for a spherical NP of radius R, the envelope of the temperature evolution varies as $1/r^3$ for $r \gg R$, while it can be approximated by a stretched exponential at the vicinity of the NP (for $r \gtrsim R$) [6]:

$$F(r) = \exp\left[-\left(\frac{r-1}{r_0}\right)^n\right] \tag{23}$$

where the fit parameters are $n = 0.45$ and $r_0 = 0.060$.

Finally, the thermodynamics is also influenced by the pulsation rate f of the laser. If f is too high, the particle may not have time to completely cool down between two successive pulses [6, 39]. This leads to a regime where the NP is permanently hot, as seen in Fig. 6. A temperature profile in $1/r$ is thus expected around the NP, despite of the pulsed illumination. In practice, such a regime is achieved when $f \gtrsim 1/\tau_{tr}$. To discriminate between both regimes, a dimensionless number ξ can be introduced such that $\xi = f\tau_{tr}$ [6]. For $\xi \ll 1$, a temperature confinement (in $1/r^3$) can be expected. Otherwise, an extended $1/r$ profile may be dominant.

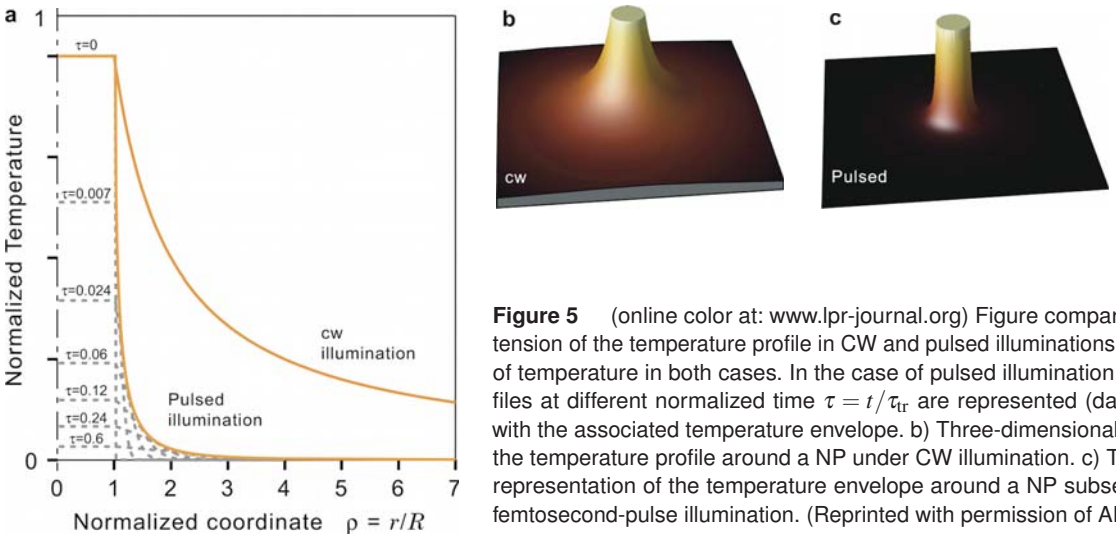

Figure 5 (online color at: www.lpr-journal.org) Figure comparing the spatial extension of the temperature profile in CW and pulsed illuminations. a) Radial profiles of temperature in both cases. In the case of pulsed illumination, temperature profiles at different normalized time $\tau = t/\tau_{tr}$ are represented (dashed lines) along with the associated temperature envelope. b) Three-dimensional representation of the temperature profile around a NP under CW illumination. c) Three-dimensional representation of the temperature envelope around a NP subsequent to a single femtosecond-pulse illumination. (Reprinted with permission of APS.)

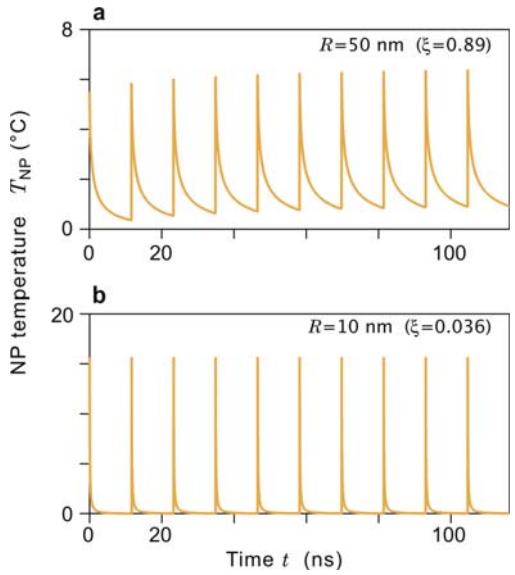

Figure 6 (online color at: www.lpr-journal.org) Temporal evolution of the temperature of a spherical gold NP of radius R illuminated by a train of pulses with a repetition rate $f = 86$ MHz and average irradiance $I = 1$ mW/μm^2: a) $R = 50$ nm; b) $R = 10$ nm.

3. Methods in thermo-plasmonics

Along with the growing interest in thermo-plasmonics, much effort has recently been put into developing a set of numerical and experimental methods to answer questions such as: What is the actual temperature increase of a plasmonic structure under illumination? What does the temperature profile look like in its surrounding medium? This section is devoted to the introduction of these numerical and experimental techniques.

3.1. Numerical methods

Investigating theoretically the thermodynamics of plasmonic NPs requires numerical frameworks coupling optics and thermodynamics. Three such hybrid numerical techniques have recently been developed. In this section, we give a brief overview of their respective principles and specificities.

The boundary element method (BEM) developed by García de Abajo and Howie in 2002 is a fully optical numerical method able to compute both the near-field and far-field optical response of plasmonic nanostructures [49]. The power of this technique relies on meshing the boundaries of the system, making it particularly fast. Although more suited for objects with axial symmetry, it also applies to arbitrary shapes when combined with more sophisticated meshing [50]. However, it cannot account for the influence of a substrate or more complex dielectric environments. Recently, the BEM has been extended to address problems in thermo-plasmonics as well. In particular, it was used to compute the steady-state temperature distribution inside and outside NPs under CW illumination (Fig. 7a) [13].

The discrete dipole approximation (DDA) and Green dyadic tensor (GDT) methods are two closely related methods that have also been intensively used to compute the far-field and near-field optical properties of metallic nanoobjects [51–53]. They require a meshing in volume, which is more memory-consuming than the BEM, but have no limitation regarding the geometry of the object, and can account for the presence of a planar substrate. The optical DDA and GDT methods have recently been extended to allow the computation of the steady-state temperature field under CW illumination (Fig. 7b–d) [15]. The influence of a substrate on the temperature distribution can also be taken into account.

The two techniques mentioned above are dedicated to steady-state simulations. Modeling transient evolutions is more difficult. Yet, it is of fundamental importance, e. g. in the case of pulsed illumination. Several theoretical approaches have been developed to address such a time-dependent problem, some of them being based on approximate analytical expressions [21, 22, 54, 55], some others based on numerical simulations [6, 39, 55, 56]. In order to precisely describe the electron and phonon dynamics

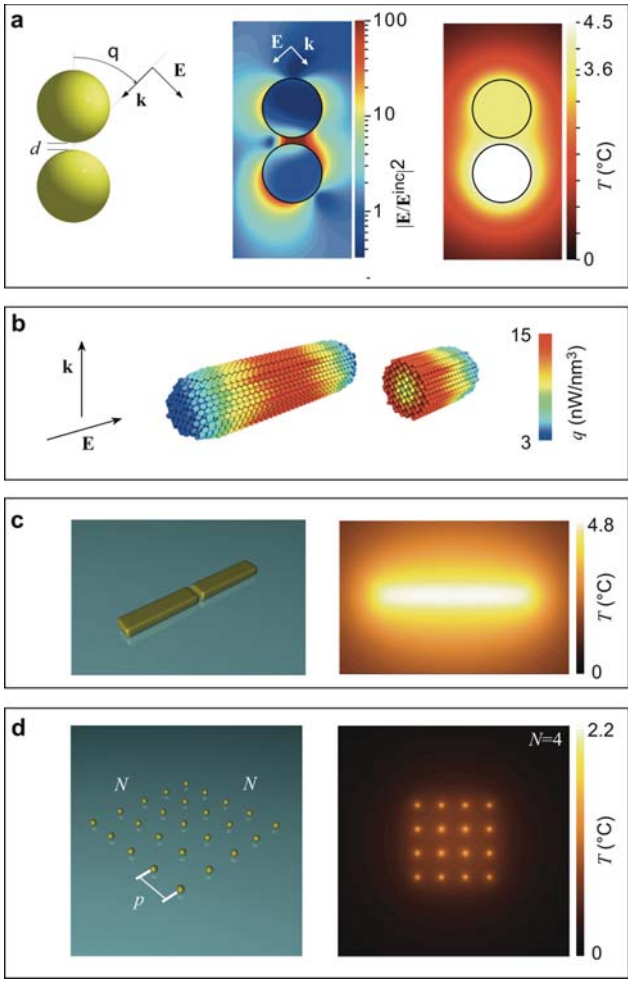

Figure 7 (online color at: www.lpr-journal.org) Overview of some numerical calculations in thermo-plasmonics. a) Computation of the electromagnetic and temperature near fields close to a gold dimer using the BEM [13]. (Reprinted with permission of ACS.) b) Computation of the heat power density inside a gold nanorod using the GDT method [12]. (Reprinted with permission of APS.) c) Computation of the temperature profile around a gold nano-antenna using the GDT method [15]. (Reprinted with permission of APS.) d) Computation of the temperature distribution around an array of spherical gold NPs using the DDA method [15]. (Reprinted with permission of APS.)

under pulsed illumination, it is usually necessary to consider in the formalism two temperatures: the electronic temperature and the phonon temperature (see Section 2.4). Indeed, these two temperatures are not necessarily equal during the transient evolution because the system is not in equilibrium. This approach is referred to as the two-temperature model (TTM) [45, 46, 57, 58].

3.2. Thermal microscopy techniques

While the use of metallic NPs as nano-sources of heat was initiated a decade ago, techniques to probe the actual resulting temperature distribution have only been developed very recently. Probing temperature at the nanoscale is fundamentally a complicated task mainly because of the non-propagative nature of heat.

In 2009, Baffou et al. mapped for the first time the temperature distribution around plasmonic NPs using an optical technique based on molecular fluorescence polarization anisotropy (FPA) measurements [59]. In this approach, fluorescent molecules are dispersed in the fluid surrounding the NPs and illuminated by linearly polarized light. Because each molecular dipole is randomly oriented, the emitted fluorescence of an ensemble of illuminated molecules is partially depolarized. When the medium surrounding the NPs gets hot, the rotational Brownian motion of the molecules is accelerated, which tends to further depolarize the emitted fluorescence as the molecules rotate more during their fluorescence lifetime [60]. Incidentally, to optimize the sensitivity of the technique, the rotational correlation time of the molecule in the host liquid should match the fluorescence lifetime of the molecule. This matching can for instance be achieved using fluorescein molecules dispersed in a mixture of water and glycerol (1:4 w/w) [59]. The resulting variation of FPA as a function of temperature is shown in Fig. 8a. This technique is able not only to map the temperature, but also the heat power density $q(r)$. In this approach, the distribution of $q(r)$ is retrieved by probing the temperature increase as function of the heating laser location. An example of $q(r)$ measurement around a lithographic gold gap antenna is presented in Figs. 8b and c [10]. In this example, it is evident that the maximum heat generation surprisingly arises from the central part of the antenna under *transverse polarization*, meaning that thermal and optical hot spots usually do not coincide.

The main advantage of this approach compared with previous fluorescence-based thermal imaging techniques is that FPA is not dependent on fluorescence intensity. Consequently, it is not affected by photobleaching, blinking, variation in the concentration of fluorophores or variation in the laser power. Recently, the same group proposed extending the technique to a biological environment using green fluorescent protein (GFP) [61]. GFP is indeed significantly larger than conventional fluorescent molecules like fluorescein making its rotational Brownian motion in water quite slow and commensurable with its fluorescent lifetime. Because of this property, those authors managed to map for the first time the temperature inside living cells with a spatial resolution of about 250 nm and a temperature accuracy of less than 1 K.

Another optical microscopy technique has been introduced that aims at characterizing the heat generation arising from nanostructures [62] This approach is based on the thermally induced optical index variation of the medium surrounding the source of heat (Fig. 8d). The measurement is achieved using a regular CCD camera combined with a modified Hartmann diffraction grating. Such a simple association makes this technique straightforward to implement on any conventional microscope with its intrinsic broadband illumination. Its spatial resolution reaches the diffraction limit and temperature variations as small as 1 K can be detected. Beyond its fast readout, the advantage of this ap-

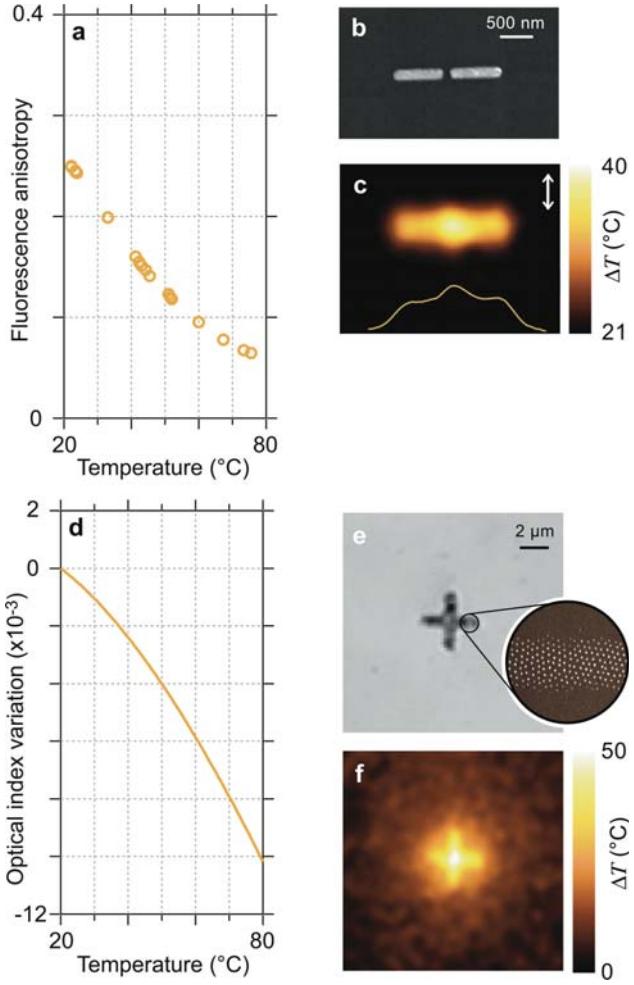

Figure 8 (online color at: www.lpr-journal.org) a) FPA–temperature calibration curve for fluorescein molecules in a glycerol–water mixture (4:1 w/w). b) Scanning electron microscopy image of a lithographic gold gap antenna and c) associated temperature map of the structure under illumination. d) Optical index of water as function of temperature. e) Optical image of a structure composed of a pattern of gold nanospheres as shown in the inset and f) associated temperature map of the structure under illumination.

proach is that it does not require one to tag the system with any marker. This approach allows one to map both the temperature and the heat power density, in a quantitative manner. An example of steady-state temperature measurement is presented in Fig. 8f. It was performed on a cross-like pattern composed of a quasi-hexagonal lattice of gold nanodots.

Richardson's group introduced an alternative optical method to determine the temperature distribution around photo-heated metal NPs. The approach consists of depositing the NPs on a thin film of AlGaN doped with Er^{3+} ions. The Er^{3+} ions are excited with 532 nm laser light and the photoluminescence spectrum recorded in each point of the image. The temperature is then retrieved by monitoring the intensity ratio of two peaks of the spectrum, corresponding to two well-defined energy transitions. This ratio is known to be temperature dependent according to the Arrhenius law. Using this technique, it was possible to map the temperature around NPs from 40 to 120 nm in size.

In 2006, de Wilde and co-workers introduced a microscopy technique called thermal radiation scanning tunneling microscopy (TRSTM) [63]. Using a near-field scanning optical microscope, those authors managed to map the surface waves supported by a SiC microstructure excited by heating the sample. In the case of polar dielectric materials, the surface waves are called surface phonon polaritons (SPhPs) and their physics is similar to the physics of surface plasmons in the visible spectral range [64]. Such a thermal-assisted SPhP excitation is possible when the SPhP resonance frequency matches the frequency of the blackbody radiation related to the sample temperature according to Wien's displacement law. A SiC–air interface features a SPhP resonance at 10.6 μm [63] that was excited by heating the sample at 170 °C. This technique markedly differs from the previously cited thermal imaging techniques: although based on thermal processes, TRSTM remains an optical technique probing an optical field. In TRSTM, heat is converted into light (through blackbody radiation), while in thermo-plasmonics the opposite transduction pathway is usually considered: light is converted into heat to produce localized thermal sources. In 2009, the Brongersma group extended the concept of thermal-assisted SPhP excitation by using SiC *nanostructures* that support *localized* surface phonons (the equivalent of LSPs in metal NPs). This interesting approach illustrates the concept of thermal-assisted optical antenna emitters working in the infrared range, a wavelength window where sources are less readily available [65].

4. Applications

A nano-source of heat is certainly one of the most fundamental tools from which science can benefit to investigate some of the most intimate processes in nature. The high level of heat control at the nanoscale achieved by plasmonic NPs provides scientists with a powerful tool that has already been exploited in a variety of fields. The aim of this section is to review some of the most active applications of thermo-plasmonics. Most of these applications are based on the use of *gold* NPs [67]. The predominance of gold over other noble metals is justified by its unique combination of advantages: (i) gold leads to resonances that can be tuned from the visible to the NIR, by adjusting the size and the shape of the NPs; it is thus well suited for applications in biology since tissues are less absorbent in the NIR range; (ii) gold offers rich and simple surface chemistry that allows functionalization of gold NPs with a variety of chemical compounds; (iii) the oxidation of gold remains very weak; and (iv) gold is not cytotoxic [68–70].

4.1. Plasmonic photothermal therapy

Photothermal therapy uses photothermal nano-agents to treat disease by local hyperthermia [71–75]. In the specific

case of cancer, the main idea of this emerging therapy is to artificially enhance the optical absorption contrast between cancerous and healthy tissues. This way, a suitable illumination enables specific photo-damage of cancer tissues without affecting the healthy surrounding. Among available photothermal agents, plasmonic NPs are very good candidates to achieve photo-damage using moderate laser intensity.

To eventually end up with an efficient treatment using gold NPs, several requirements have to be fulfilled. First, gold NPs need to be specifically delivered to the cancer cells in order to limit the heat generation to the malignant tissues and not to the surrounding healthy tissues. Targeting of cancer cells with gold NPs can be either passive or active [73]. The passive approach exploits the fact that, due to their rapid growth, cancer cells are endowed with vasculatures (up to 2 µm in size) that facilitate NP uptake. Additionally, the lymphatic drainage of tumors is reduced compared with healthy tissues, making it harder for NPs to leave the tumor once they get into it. In the active approach, targeting of cancer cells is achieved by coating the NP surface with antibodies, proteins or other ligands that have a specific binding affinity with receptors overexpressed at the membrane of cancer cells.

The second aspect that has to be considered is the wavelength of the incident light used to heat the NPs. Indeed, light absorption of human tissues is minimum in the so-called transparency window (between 700 and 900 nm). Working in this region of the spectrum allows reaching tumors that can be up to several centimeters deep, along with minimum absorption and thus less heating from the rest of the exposed tissues that are not targeted with NPs. While light absorption of spherical gold NPs peaks in the green, LSP resonances can be shifted to the infrared by using non-spherical NPs. This explains why hyperthermia experiments are mainly based on the use of gold nanoshells [74, 76–78] (formed by a dielectric core surrounded by a thin gold layer), gold nanorods [79] or gold nanocages [80], which allow accurate tuning of LSPs to the NIR spectral region. In some cases, the use of spherical gold NPs can also be efficient due to agglomeration of NPs that tends to red-shift the NP absorption spectrum [81–83].

In the original work introducing the use of gold NPs for plasmonic photothermal therapy (PPTT), Hirsch and co-workers used human breast carcinoma cells incubated with gold nanoshells *in vitro* [84]. The cells were found to have undergone photothermally induced morbidity upon exposure to NIR light (820 nm, 35 W/cm^2). Conversely, cells without nanoshells displayed no loss in viability using the same NIR illumination conditions. Also, exposure to low doses of NIR light (820 nm, 4 W/cm^2) in solid tumors treated with metal nanoshells reached average maximum temperature increases capable of inducing irreversible tissue damage ($\Delta T = 37.4 \pm 6.6$ °C) within 4–6 min. Importantly, controls treated without nanoshells demonstrated significantly lower average temperature increase on exposure to NIR light ($\Delta T < 10$ °C). Shortly after [85], the feasibility of this approach was successfully tested *in vivo* on a mouse model. Gold nanoshells coated with polyethylene glycol (PEG) were intravenously injected into mice. The tumor was then illuminated with a diode laser over sessions of 3 min. After 10 days of treatment, complete resorption of the tumor was observed. More than 90 days after the treatment, all treated mice remained healthy and free of tumors. At about the same time, Pitsillides et al. proposed to use nanosecond-pulsed laser irradiation for more efficient PPTT [86]. This series of experiments was performed in the visible range using spherical gold NPs. Those authors demonstrated that when using pulsed laser illumination, the brief but intense temperature increase following a short laser pulse yields a fast vaporization of a thin layer around the NPs causing more efficient cancer cell denaturation as compared with CW illumination. The use of gold nanorods was first proposed by the El-Sayed group a few years later [79]. In 2008, Stern et al. carried out NP-based laser ablation on an apparent subcutaneous tumor around 1 cm in diameter (Fig. 9) [66]. In this work, gold NPs were introduced by

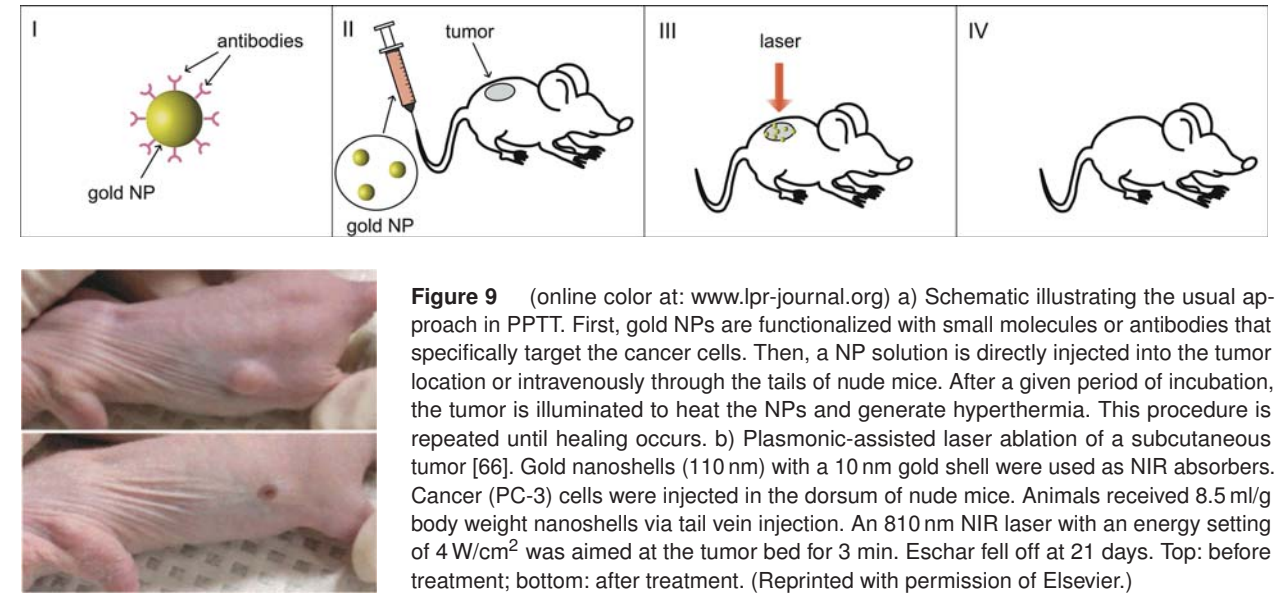

Figure 9 (online color at: www.lpr-journal.org) a) Schematic illustrating the usual approach in PPTT. First, gold NPs are functionalized with small molecules or antibodies that specifically target the cancer cells. Then, a NP solution is directly injected into the tumor location or intravenously through the tails of nude mice. After a given period of incubation, the tumor is illuminated to heat the NPs and generate hyperthermia. This procedure is repeated until healing occurs. b) Plasmonic-assisted laser ablation of a subcutaneous tumor [66]. Gold nanoshells (110 nm) with a 10 nm gold shell were used as NIR absorbers. Cancer (PC-3) cells were injected in the dorsum of nude mice. Animals received 8.5 ml/g body weight nanoshells via tail vein injection. An 810 nm NIR laser with an energy setting of 4 W/cm^2 was aimed at the tumor bed for 3 min. Eschar fell off at 21 days. Top: before treatment; bottom: after treatment. (Reprinted with permission of Elsevier.)

passive targeting via tail vein injection. Measurements were carried out on 46 tumors separated in 6 different groups corresponding to different conditions. Tumor necrosis or regression of 93% was observed for the group of mice that received 8.5 ml/g body weight, while the tumors of the mice that received a saline solution instead kept growing despite identical illumination conditions. In this work, the need for NP accumulation was emphasized. No discernible toxicity attributable to the gold NPs was identified. Since then, numerous studies have been carried out to push this initial proposal towards clinical trials [74]. Special attention has been given to investigating new particle geometries and their specific targeting to cancer cells. In recent years, the company Nanospectra (www.nanospectra.com) has initiated some clinical tests on head and neck cancer using gold nanoshells.

4.2. Nano-surgery

Laser surgery, which consists of using laser light to cut tissues, has become a reliable alternative to the conventional scalpel in fields such as ophthalmology and dermatology [87, 88]. It offers bloodless and more accurate cutting along with reduced risks of infection.

At a smaller scale, laser light can be used as a tool to assist transfection of individual cells by forming a transient pore in the cell membrane [89] that permits the introduction of either therapeutic agents (proteins, DNA, RNA) or imaging agents (fluorophores, quantum dots, nanoparticles) through the cell membrane and as a tool to cut individual neurons [90].

Optical transient poration in cell membranes has been demonstrated using a variety of illumination conditions, involving different mechanisms depending on the laser–cell interaction [91]. While CW illumination mainly induces a local heating at the cell membrane, femtosecond pulsed illumination with high repetition rate induces membrane permeability that is mainly the result of a low-density plasma originating from the generation of free electrons.

Interestingly, this technique permits the study of one cell at a time. However, it suffers from potential photo-damage originating from the high laser power that is required. In this context, the use of plasmonic NPs makes it possible to locally increase the absorption and thus reduce the intensity requirements. Also, the possibility of controlling heating near few to single particles is expected to significantly reduce the dimension of the pore.

Along this line, Urban and co-workers have recently proposed the use of a single gold NP, trapped at the focus of a CW green laser, to perforate phospholipid membranes (Fig. 10) [92]. In their experiment, an 80 nm spherical gold NP was trapped and brought to a vesicle membrane. By increasing the laser intensity, the particle was heated until it crossed the membrane and penetrated the vesicle. The resulting pore was a few hundreds of nanometers in size and remained open for several minutes.

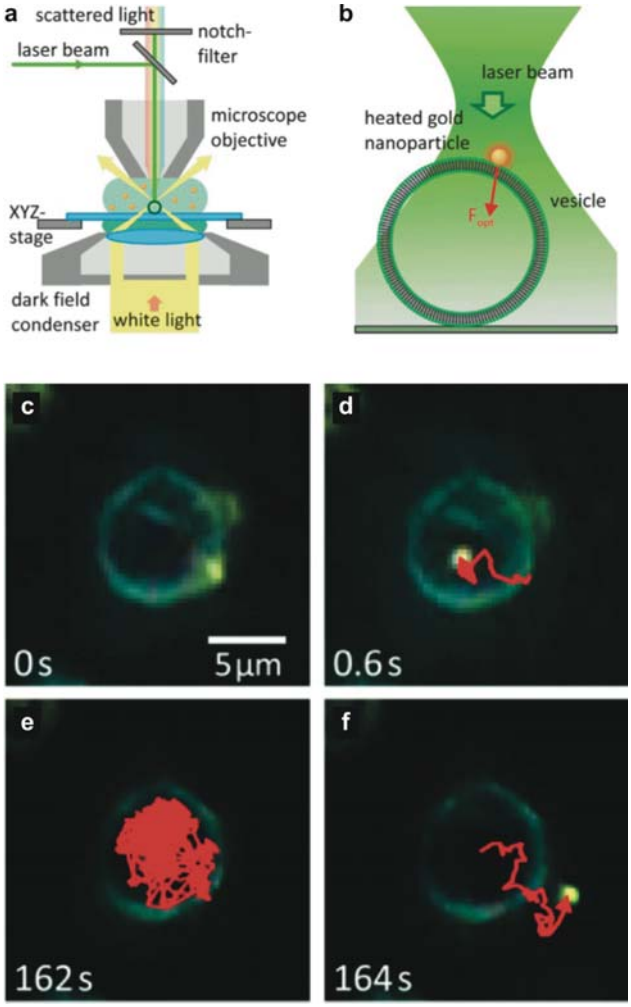

Figure 10 (online color at: www.lpr-journal.org) Illustration of the perforation of a phospholipid membrane using a trapped single gold NP. a) Schematic of the experimental setup used for optical injection and imaging [92]. b) Gold NPs are attached to the membrane of giant unilamellar vesicles prior to injection. The laser is defocused, resulting in a spot size of 6 µm at the focal plane of the microscope objective. c) A dipalmitoylphosphatidylcholine vesicle before injection of a gold NP attached to the membrane. d,e) Tracking of the movement of the gold NP (red trace) shows it is confined to the inside of the vesicle. f) Often, after a certain time, the NP was observed leaving the vesicle at the same position at which it was injected. This suggests that the injection process forms a pore in the gel-phase membrane. (Reprinted with permission of ACS.)

4.3. Plasmonic photothermal delivery

Another biomedical application in thermo-plasmonics focuses on targeted delivery of drugs or genes for therapeutic purposes. The therapeutic agents are attached to gold NPs that act as nano-carriers through the human body. Once at the desired location, the active agents can be detached and released by remotely heating the NPs using laser illumination [93–95]. Hence, in this kind of application, plasmonic NPs have two roles: they act as both nano-carriers and

nano-sources of heat. This approach allows unprecedented control of the location, the timing, the duration and the magnitude of drug release. Sufficient incident light intensity must be used to release drugs or nucleotides, but must remain below the intensity threshold causing photothermal damage of cells and tissues [96]. Plasmonic photothermal delivery (PPTD) has been demonstrated using various geometries of plasmonic systems, such as nanospheres [97–100], nanorods [101–104], nanoshells [105], nanocages [106] and liposomes [107–109], as described below.

In 2005, the Yamada group demonstrated the feasibility of PPTD by using NIR pulsed radiation to remotely control gene expression in specific Hela cells [110]. Those authors used gold nanorods functionalized with the gene related to the expression of GFP. Efficient gene release and expression was evidenced by monitoring the expression of GFP inside cells. Induced GFP expression was specifically observed in cells that were locally exposed to NIR radiation. In this work, the gene release was triggered by a morphological change of the NPs: under illumination, the nanorods melt and turn into spheres, which markedly reduces the NP interface available for keeping DNA strands attached. In 2006, the El-Sayed group used femtosecond-pulsed illumination at $\lambda_0 = 400$ nm combined with complexes formed by DNA strands covalently attached to spherical gold NPs [98]. Since no shape modification is expected in that case, it was suggested that gold–sulfur bond breaking is not only triggered by local heating but also by the transfer of hot electrons created within the metal. Another PPTD approach was proposed for the first time in 2007 by Paasonen et al. [107]. The idea was to use liposomes that can release their content under pulsed illumination. Gold NPs were incorporated into the lipid bilayer or the core of the liposomes to generate the photothermal effect required to induce the phase transition of the phospholipid membrane and its permeability. This approach can be advantageous as it can potentially make the drug delivery mechanism biologically more compatible. The use of liposomes or gold nanocages permits the conveyance of the therapeutic agent on the inside of the nano-carrier, as a cage.

In most of the PPTD experiments, the actual photoactivated process responsible of the release is not well identified. Recent experiments performed by the Halas group on gold nanoshells and nanorods aimed at discriminating the respective contribution of heat and hot electrons to the release mechanism in PPTD. It was shown that these contributions depend on the geometry of the NPs [105, 111]. In 2009, the Halas group used gold nanoshells and a CW infrared laser to release single-strand DNA. In such an approach the dehybridization and release of DNA were triggered by the temperature increase of the medium surrounding the NPs [105]. In 2011, by comparing PPTD using gold nanorods and nanoshells, the same group came up with the conclusion that non-thermal mechanisms may play a role in plasmon resonant, light-triggered DNA release.

In 2011, the Lapotko group proposed a novel PPTD approach that takes advantage of the formation of transient nanobubbles generated by gold NPs heated under pulsed illumination [100]. These nanobubbles could briefly open the cellular membrane and create an inbound transient jet that could inject extracellular molecules into individual specific cells without damaging them.

4.4. Photothermal imaging

When a metal NP is illuminated, the temperature increase experienced by the surrounding medium induces a local variation of refractive index. In 2002, Boyer et al. [112] took advantage of this effect to develop an optical microscopy technique aimed at detecting metal NPs ($\sim$10 nm) that are normally too small to be detected using any conventional optical microscopy. The local variation of the refractive index, also known as the nanolens effect [113], was detected by measuring the phase difference between two separated beams of an interferometer. One of the two beams propagates through the heated region while the other one serves as a reference. An improved signal over noise is achieved by modulating the heating laser using an acousto-optic modulator.

This approach originally led to the detection of 10 nm NPs, provided that their associated temperature increase reached $\sim$15 K. In this context, metallic NPs turn into efficient contrast agents that overcome many drawbacks of conventional fluorescent markers, such as autofluorescence, blinking, bleaching or fluorescence saturation. In 2003, Cognet and co-workers demonstrated that this technique could have valuable applications in biology [114]. Those authors managed to visualize single membrane proteins labeled with 10 nm gold NPs in fixed COS7 cells. Because of the absence of photobleaching, the proteins can be visualized for arbitrarily long times, offering new opportunities for efficient protein tracking in three dimensions. This is a great advantage compared with regular fluorescent markers, which tend to photobleach very rapidly in tracking experiments. However, the authors pointed out that the high temperature increase required to obtain reasonable signal-to-noise ratio can induce damage to living biological systems. In 2004, Berciaud and co-workers solved this issue by improving the sensitivity by two orders of magnitude using heterodyne detection [115]. Using this new approach, gold NPs smaller than 5 nm could be detected with an associated local temperature increase of only 1 K. Such an achievement opened the path to experiments in living cells: in 2006, the same group reported on the real-time two-dimensional tracking of membrane protein in living COS7 cells and neurons [116], and later of mitochondria [117]. In 2010, the Orrit group investigated the detection limit in photothermal microscopy. Those authors managed to detect a dissipated power of 3 nW from a single gold NP with a signal-to-noise ratio of 8, and an integration time of 10 ms. This corresponds to a less than 0.1 K surface temperature rise for a 20 nm diameter gold nanosphere (0.4 K for 5 nm) (Fig. 11). Very recently, the same group managed to push the sensitivity of this method by detecting single dye molecules instead of gold NPs [119].

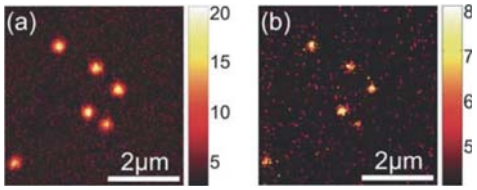

Figure 11 (online color at: www.lpr-journal.org) Photothermal imaging of 20 nm gold NPs in glycerol using a heating laser power of a) 9 μW (3 ms exposure time) and b) 1 μW (10 ms). Dissipated powers and temperature rises are 24 and 2.6 nW, and 0.7 K and 80 mK, respectively [118]. (Reprinted with permission of RSC.)

4.5. Photoacoustic imaging

In order to enable the early detection of cancerous lesions *in situ*, medical imaging techniques have to combine high resolution, high detection depth and high specificity to malignant tissues. On the one hand, optical imaging techniques usually provide a good contrast, but low resolution and penetration depth due to the diffusive nature of biological tissues. On the other hand, acoustic imaging techniques (like ultrasonography) lead to high penetration depth and resolution due to the relatively unhindered propagation of ultrasonic waves. However, such a full-acoustic approach suffers from a low contrast between different tissues with similar acoustic properties.

Photoacoustic (PA) (or optoacoustic) tomography combines the advantages of light and ultrasound to achieve the detection of deep tumors with high resolution (< 1 mm) and contrast [120, 121]. The basis of PA tomography is the generation of acoustic signals using short laser pulses. Working with NIR light ensures a maximal light penetration in tissues. The absorption of a focused pulsed laser generates a rapid and localized temperature increase (< 1 °C). The subsequent thermal-induced expansion of the tissue triggers the formation and propagation of an acoustic wave (or stress wave) that can be detected at the surface of the body by using an array of ultrabroad-band acoustic transducers. Finally, a deconvolution algorithm is used to render a three-dimensional image of the absorbing tissues. Since hemoglobin usually has orders of magnitude larger absorption than surrounding tissues, PA imaging is often used to visualize blood vessels or abnormal angiogenesis (formation of new blood vessels from existing ones) in advanced tumors. Low acoustic attenuation allows the detection of tumors 5 to 6 cm deep, typical of breast or prostate cancers. The duration and time of arrival of the acoustic signal to the ultrasonic detector reveals the size and location of the target.

In early stages of disease, however, angiogenesis is not sufficient to differentiate cancer tissues from healthy ones. The use of plasmonic NPs as efficient photo-absorbers to enhance PA contrast was first proposed in 2004 by Copland et al. [121]. Those authors demonstrated the concept by performing *in vitro* experiments on breast cancer cells embedded in a gelatin phantom designed to mimic breast tissue. Spherical 40 nm gold NPs were bound to the cancer cells via active targeting. In 2007, the first gold-NP-assisted PA signal *in vivo* was reported by the same group [122]. In this work, gold nanorods were used to enhance the photothermal contrast in the infrared region and were simply injected subcutaneously at a specific region in a mouse. In 2009, Zhang and co-workers conducted passive targeting experiments on living mice [123]. The authors used PEGylated spherical gold NPs injected via the tail vein and illuminated at 532 nm. The accumulation of gold NPs in the tumor location via passive targeting was evidenced. In the same year, Wang et al. addressed a field of research different from oncology [124]. They managed to image macrophages in atherosclerotic plaques. Mouse monocytes–macrophages, which are characterized by a high rate of non-specific uptake, were incubated with PEGylated NPs overnight. Interestingly, multiple wavelength illumination was used to discriminate between NPs internalized by the microphages that accumulated to form clusters from individual NPs that were not internalized. Recently, alternative NP geometries have demonstrated enhanced PA contrast. For instance, nanocages led to an enhancement of the PA signal due to their extraordinarily enhanced absorption cross-section (Fig. 12) [125]. In the case of silica-coated gold nanorods, it was suggested that the reduction of the gold interfacial thermal resistance with the solvent due to the silica coating could contribute to a stronger PA signal [126].

Note that in PA experiments using gold NPs, the actual origin of the acoustic waves remains unclear. In particular, the possible occurrence of cavitation and bubble formation has not been clearly evidenced. The thermodynamics at the vicinity of metallic gold NPs under pulsed illumination is a very intricate problem that is still under active investigation.

4.6. Plasmon-assisted nano-chemistry

Chemical reactions are influenced by various parameters such as temperature, pH and pressure. Usually, a temperature increase is accompanied by an increase in the reaction rate as described by the empirical Arrhenius law that expresses the dependence on temperature T of the reaction rate constant K:

$$K = A\mathrm{e}^{-E_\mathrm{a}/k_\mathrm{B}T} \tag{24}$$

where A is a constant, E_a the activation energy and k_B the Boltzmann constant.

In this context, the ability of plasmonic NPs to control heat over time and space with an unprecedented level of accuracy appears naturally as a means to efficiently control chemical reactions at the nanoscale. For instance, while heating a liquid at 60 °C during only one second is difficult using conventional means, it is straightforward using gold NPs combined with laser illumination due to the small heated volume and its associated reduced thermal inertia.

In 2007, Cao et al. illustrated the concept of plasmon-assisted nano-chemistry by initiating the thermal-assisted growth of semiconducting nanowires and carbon nanotubes using gold NPs in a gas environment. By using an array of gold nanospheres and by controlling the size of the laser beam, those authors managed to fabricate an arbitrarily large pattern of organized nanowires on a planar substrate.

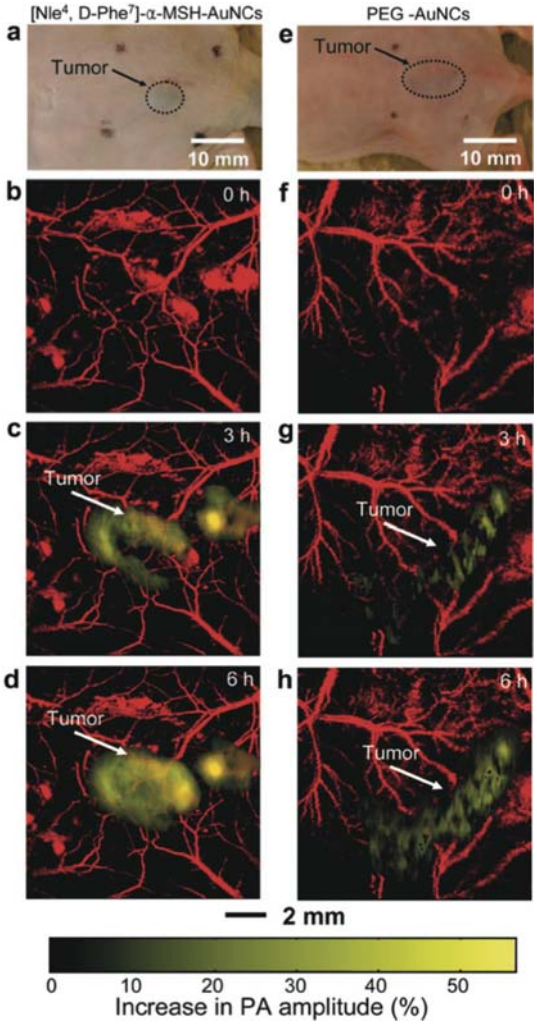

Figure 12 (online color at: www.lpr-journal.org) *In vivo* non-invasive PA images of B16 melanomas using gold nanocages [125]. Photographs of nude mice transplanted with B16 melanomas before injection of a) bioconjugated and e) PEGylated nanocages. PA images of the B16 melanomas after intravenous injection with 100 µl of 10 nM b–d) bioconjuated and f–h) PEGylated nanocages through the tail vein. Color scheme: red, blood vessels; yellow, increase in PA amplitude. (Reprinted with permission of ACS.)

In 2009, Adleman et al. reported on the formation of CO_2 and H_2 bubbles around a pattern of photo-heated gold NPs immersed in a water–ethanol mixture. Although those authors presented their work as plasmon-assisted catalysis, no catalytic activity of gold was evidenced in this experiment, strictly speaking. However, this work nicely illustrates the ability to create not only a temperature increase, but also a high-pressure environment around the NPs. Indeed, the formation of a bubble comes along with a substantial increase of the inner pressure P_{in} due to the very small radius of curvature R of the bubble according to $P_{in} = P_{out} + 2\gamma/R$, where γ is the surface tension ($\gamma \approx 72$ mN/m at 25 °C). To give an order of magnitude, a 3 µm bubble features an inner pressure of 2 bar while surrounded by water under 1 bar. Remarkably, the temperature and pressure that can be obtained at the vicinity of a gold NP under illumination are thus comparable to those obtained in heavy and bulky reactors used in industry. Recently, the Richardson group reported on the observation of water superheating around a gold NP up to almost 600 K without bubble formation [127]. This unexpected thermodynamic behavior is due to the nanometric size of the source of heat. More recently, Christopher et al. claimed that low-intensity CW illumination of silver NPs yields hot electrons that can be used, in tandem with photothermal energy, to drive/catalyze commercially relevant chemical reactions and achieve viable rates under significantly reduced temperatures [128]. Note that gold NPs can also be used in principle to enhance *photo*-induced chemical reactions due to the enhanced optical fields achieved close to metal structures. This aspect is beyond the scope of this review and will not be discussed herein.

4.7. Plasmon-assisted optofluidics

Accurate manipulation of fluids in integrated micrometric channels, known as microfluidics, is a fast-growing field that has become a key ingredient in the development of future miniaturized analytical devices. There is much current expectation for incorporating in a microfluidic platform all necessary components and functionalities to achieve a lab-on-a-chip capable of performing parallel chemical and biological analyses. Along this direction, different approaches are considered in order to control fluid dynamics through elementary operations including fluid routing and mixing. Among the various strategies, photo-heating is attractive owing to its simplicity, its being free of any complex microfluidic designs, pumps, valves or electrode patterning. Two main thermal effects leading to light-induced fluid motion can be potentially exploited: thermocapillary forces and Marangoni convection. On the one hand, the thermocapillary force applies at a fluid–gas interface. It results from the dependence of the surface tension on the temperature. For instance, Baroud et al. managed to guide and sort droplets in microfluidics channels using a focused laser beam [129]. On the other hand, Marangoni convection is characterized by an upward (Archimedes) fluid convection resulting from a decrease of the mass density of the fluid under heating.

Once again, using plasmonic nanostructures for this purpose appears as the most natural means to enlarge the potential of this field of research. In 2005, Farahi et al. proposed enhancing the thermocapillary effect by using a surface plasmon polariton (SPP) supported by a flat gold film [130]. More precisely, those authors managed to manipulate droplets of silicone oil and glycerol via surface tension-driven forces sustained by surface plasmon de-excitation energy. Along the same lines, Liu and co-workers proposed an approach in which fluid heating was enhanced by dispersing plasmonic NPs in the liquid (Fig. 13) [131]. In their experiment, the fluid was pulled at velocities as high as 500 µm/s within a microfluidic channel by displacing the laser beam. This approach was also successfully used to route fluids at microfluidic junctions.

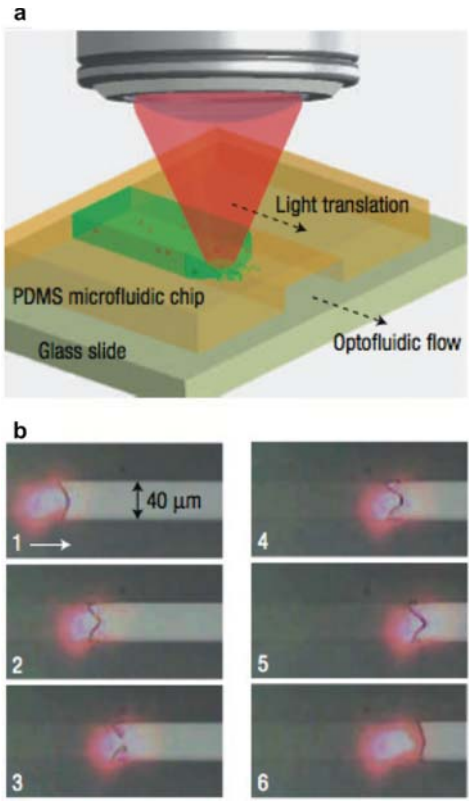

Figure 13 (online color at: www.lpr-journal.org) LSP-assisted optofluidic control in straight microfluidic channels [131]. a) Illustration of the experimental system configuration. b) Optofluidic control in a 40 µm wide channel. The video prints show that the flow of the fluid containing gold NPs follows the optical guiding of a 10 mW, 785 nm laser spot at a speed of ∼50 µm/s (frames 1–5) and stops otherwise (frame 6). (Reprinted with permission of NPG.)

Moving a fluid through microscale thermal-induced convection using a gold nanostructure (Marangoni convection) has been investigated experimentally by Garcés-Chávez and co-workers. Those authors demonstrated that Marangoni convection (combined with thermophoresis) induced by a SPP at a flat gold film can be used to self-assemble a large number of colloidal microparticles on a substrate [132]. Similarly, Miao et al. achieved fluid mixing near a surface patterned with a monolayer of plasmonic NPs supporting LSP [133]. Recently, Donner and co-workers have theoretically studied the photothermally induced fluid convection around plasmonic structures [134]. In particular, all the orders of magnitude of temperature and fluid velocity were discussed as a function of the morphology of the plasmonic structure and the illumination conditions (Fig. 14). Characteristic temperature, velocity, spatial scales and time scales depend on the dimensions of the plasmonic structure and on the delivered heat. For instance, the resulting characteristic fluid velocity at the vicinity of the structure is given by

$$\tilde{V} \sim R^2 \rho \beta g \delta T / \eta \qquad (25)$$

where g is the gravitational acceleration, δT the temperature increase of the structure, β the dilatation coefficient of water

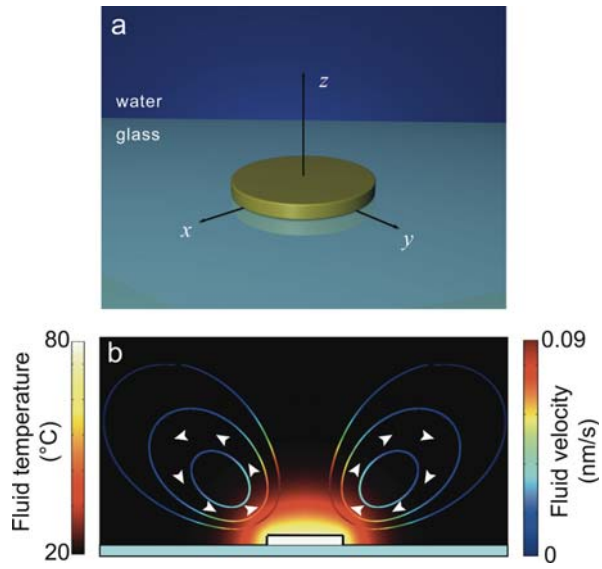

Figure 14 (online color at: www.lpr-journal.org) Thermal-induced fluid convection using a single gold disc. a) Representation of the system: a gold disc, 500 nm in diameter and 40 nm thick, immersed in water. b) Side view of the temperature distribution and the thermal-induced fluid velocity field of the fluid surrounding the gold nanodisc (numerical simulations) [134]. (Reprinted with permission of ACS.)

and η the dynamical fluid viscosity. While the fluid velocity is negligible (< 10 nm/s) for nanometer-sized structures due to a very small Reynolds number, it plays a significant role for either micrometer-sized plasmonic structures or assemblies of nanostructures. Note that, at the considered scales, equilibrium is reached very fast, typically after 1 ns to 1 µs, depending on the size of the structure but not on the temperature increase.

5. Prospects

In this review, we have presented recent advances in the field of thermo-plasmonics. This recent and fast-growing discipline has now applications in many areas of science. While metallic NPs have been for long mainly used for their optical properties, they have recently triggered much expectation for enhancing thermal-induced processes in areas such as medical therapy, imaging in biology, hydrodynamics and chemistry.

The understanding of the physics associated with heating of metal NPs is still a matter under active investigation. The interplay between optics and thermodynamics considerations makes their modeling intricate. In particular, some physical effects involved under pulsed illumination are still enigmatic. Also, the small number of available thermal imaging techniques capable of probing the temperature near plasmonic structures has so far drastically limited advancing the field. Macroscopic photothermal effects such as tissue damage, fluid convection, chemical reactions or drug release were undoubtedly evidenced, but the actual temperature of

the NPs during these processes was often unknown. In that sense, the recent developments of efficient thermal imaging techniques are expected to contribute to further insight.

All the applications of thermo-plasmonics presented in this review feature different degrees of progress. While applications such as photothermal cancer therapy have already led to clinical trials, areas such as plasmonic-assisted nanochemistry or microfluidics are still at an early stage of development. Other promising areas of research, not presented in this review, are even more conceptual, like plasmon-assisted magnetic recording [135,136], phononics [137–139] or thermal microbiology at the single-cell level. Much effort is currently devoted to the development of these fields.

All this recent progress and unresolved questions promise exciting forthcoming developments in the near future that will continue the exciting story of thermo-plasmonics.

Acknowledgements. This work was supported by the European Commission's Seventh Framework Programme under Grants SPEDOC (248835), ERC-Plasmolight (259196), and Fundació Privada CELLEX.

Received: 12 January 2012, **Revised:** 24 February 2012, **Accepted:** 6 March 2012

Published online: 24 April 2012

Key words: Plasmonics, nano-optics, thermodynamics, biophysics.

Guillaume Baffou studied physics at the Ecole Normale Suprieure de Cachan and University Paris XI (France). He got his Ph.D. in 2007 from the University Paris XI on the study of light emission in scanning tunneling microscopy. He then spent 3 years at ICFO, the Institute of Photonic Science (Castelldefels, Spain) as a postdoc in the Plasmon Nanooptics group. Since 2010, he is a research scientist at the Fresnel Institute in Marseille, France. His research interests include plasmonics and associated thermal effects.

Romain Quidant received his PhD in Physics in 2002 from the University of Burgundy (France). Since 2002 he has worked in Barcelona at ICFO within the field of plasmonics. In 2006, he was appointed junior Professor and group leader of the Plasmon NanoOptics group at ICFO. In 2009, he was appointed tenure Professor both at ICFO and ICREA. The same year he was also awarded the Fresnel prize from the European Physics Society for his outstanding contribution to the field of plasmon optics. In 2010 he received a Starting Grant from the European Research Council (ERC). Since 2010, he serves as the coordinator of the European FP7-STREP project SPEDOC.

References

[1] M. Pelton, J. Aizpurua, and G. Bryant, Laser Photon. Rev. **2**(3), 136 (2008).
[2] A. O. Govorov and H. H. Richardson, Nano Today **2**(1), 30 (2007).
[3] M. Grzelczak, J. Pérez-Juste, P. Mulvaney, and L. M. Liz-Marzán, Chem. Soc. Rev. **37**, 1783 (2008).
[4] C. F. Bohren and D. R. Huffman, Absorption and scattering of light by small particles (Wiley interscience, 1983).
[5] V. Myroshnychenko, J. Rodríguez-Fernández, I. Pastoriza-Santos, A. M. Funston, C. Novo, P. Mulvaney, L. M. Liz-Marzán, and F. J. García de Abajo, Chem. Soc. Rev. **37**, 1792 (2008).
[6] G. Baffou and H. Rigneault, Phys. Rev. B **84**, 035415 (2011).
[7] B. Khlebtsov, V. Zharov, A. Melnikov, V. Tuchin, and N. Khlebtsov, Nanotechnology **17**, 5167 (2006).
[8] H. Chen, L. Shao, T. Ming, Z. Sun, C. Zhao, B. Yang, and J. Wang, Small **6**(20), 2272 (2010).
[9] A. Arbouet, D. Christofilos, N. Del Fatti, F. Vallée, J. R. Huntzinger, L. Arnaud, P. Billaud, and M. Broyer, Phys. Rev. Lett. **93**(12), 127401 (2004).
[10] G. Baffou, C. Girard, and R. Quidant, Phys. Rev. Lett. **104**, 136805 (2010).
[11] A. O. Govorov, W. Zhang, T. Skeini, H. Richardson, J. Lee, and N. A. Kotov, Nanoscale Res. Lett. **1**, 84 (2006).
[12] G. Baffou, R. Quidant, and C. Girard, Appl. Phys. Lett. **94**, 153109 (2009).
[13] G. Baffou, R. Quidant, and F. J. García de Abajo, ACS Nano **4**, 709 (2010).
[14] H. H. Richardson, M. T. Carlson, P. J. Tandler, P. Hernandez, and A. O. Govorov, Nano Lett. **9**, 1139 (2009).
[15] G. Baffou, R. Quidant, and C. Girard, Phys. Rev. B **82**, 165424 (2010).
[16] R. Rodríguez-Oliveros and J. A. Sánchez-Gil, Opt. Express **20**(1), 621 (2012).
[17] A. J. Schmidt, J. D. Alper, M. Chiesa, G. Chen, S. K. Das, and K. Hamad-Schifferli, J. Phys. Chem. C **112**, 13320 (2008).
[18] O. M. Wilson, X. Hu, D. G. Cahill, and P. V. Braun, Phys. Rev. B **66**, 224301 (2002).
[19] Z. Ge, D. G. Cahill, and P. V. Braun, J. Phys. Chem. B **108**, 18870 (2010).
[20] J. Alper and K. Hamad-Schifferli, Langmuir **26**(6), 3786 (2010).
[21] V. K. Pustovalov, Chem. Phys. **308**, 103 (2005).
[22] A. N. Volkov, C. Sevilla, and L. V. Zhigilei, Appl. Surf. Sci. **253**, 6394 (2007).
[23] M. Hu and G. V. Hartland, J. Phys. Chem. B **106**, 7029 (2002).
[24] M. Hu, X. Wang, G. V. Hartland, P. Mulvaney, J. P. Juste, and J. E. Sader, J. Am. Chem. Soc. **125**, 14925 (2003).
[25] A. L. Tchebotareva, P. V. Ruijgrok, and M. Orrit, Laser Photon. Rev. **4**, 581 (2010).
[26] N. Large, L. Saviot, J. Margueritat, J. Gonzalo, C. N. Afonso, A. Arbouet, P. Langot, A. Mlayah, and J. Aizpurua, Nano Lett. **9**(11), 3732 (2009).
[27] D. Lapotko, Opt. Express **17**, 2538 (2009).
[28] E. Lukianova-Hleb, Y. Hu, L. Latterini, L. Tarpani, S. Lee, R. A. Drezek, J. H. Hafner, and D. O. Lapotko, ACS Nano **4**, 2109 (2010).

[29] A. Vogel, N. Linz, S. Freidank, and G. Paltauf, Phys. Rev. Lett. **100**, 038102 (2008).
[30] V. Kotaidis, C. Dahmen, G. von Plessen, F. Springer, and A. Plech, J. Chem. Phys. **124**, 184702 (2006).
[31] D. Lapotko, Heat Mass Transfer **52**, 1540 (2009).
[32] S. Link, C. Burda, B. Nikoobakht, and M. A. El-Sayed, J. Phys. Chem. B **104**, 6152 (2000).
[33] S. Link, C. Burda, M. B. Mohamed, B. Nikoobakht, and M. A. El-Sayed, J. Phys. Chem. A **103**, 1166 (1999).
[34] O. Warsharvski, L. Minai, G. Bisker, and D. Yelin, J. Phys. Chem. C **115**, 3910 (2011).
[35] J. Wang, Y. Chen, X. Chen, J. Hao, M. Yan, and M. Qiu, Opt. Express **15**(14726) (19).
[36] E. Lukianova-Hleb, L. J. E. Anderson, S. Lee, J. H. Hafner, and D. O. Lapotko, Phys. Chem. Chem. Phys. **12**, 12237 (2010).
[37] A. Plech, V. Kotaidis, S. Grésillon, C. Dahmen, and G. von Plessen, Phys. Rev. B **70**, 195423 (2004).
[38] E. Y. Hleb and D. O. Lapotko, Nanotechnology **19**, 355702 (2008).
[39] O. Ekici, R. K. Harrison, N. J. Durr, D. S. Eversole, M. Lee, and A. Ben-Yakar, J. Phys. D **41**, 185501 (2008).
[40] M. Hu, H. Petrova, and G. V. Hartland, Chem. Phys. Lett. **391**, 220 (2004).
[41] S. Merabia, P. Keblinski, L. Joly, L. J. Lewis, and J. L. Barrat, Phys. Rev. E **79**, 021404 (2009).
[42] S. Merabia, S. Shenogin, L. Joly, P. Keblinski, and J. L. Barrat, Proc. Natl Acad. Sci. USA **106**, 15113 (2009).
[43] P. Grua, J. P. Morreeuw, H. Bercegol, G. Jonusauskas, and F. Vallée, Phys. Rev. B **68**, 035424 (2003).
[44] H. Inouye, K. Tanaka, I. Tanahashi, and K. Hirao, Phys. Rev. B **57**, 11334 (1998).
[45] A. Arbouet, C. Voisin, D. Christofilos, P. Langot, N. Del Fatti, F. Vallée, J. Lermé, G. Celep, E. Cottancin, M. Gaudry, M. Pellarin, M. Broyer, M. Maillard, M. P. Pileni, and M. Treguer, Phys. Rev. Lett. **90**(17), 177401 (2003).
[46] W. Huang, W. Qian, M. A. El-Sayed, Y. Ding, and Z. L. Wang, J. Phys. Chem. C **111**, 10751 (2007).
[47] J. H. Hodak, A. Henglein, and G. V. Hartland, J. Chem. Phys. **111**, 8613 (1999).
[48] S. Link, C. Burda, Z. L. Wang, and M. A. El-Sayed, J. Chem. Phys. **111**, 1255 (1999).
[49] F. J. García de Abajo and A. Howie, Phys. Rev. B **65**, 115418 (2002).
[50] V. Myroshnychenko, E. Carbó-Argibay, I. Pastoriza-Santos, J. Pérez-Juste, L. M. Liz-Marzán, and F. J. García de Abajo, Adv. Mater. **20**, 4211 (2008).
[51] C. Girard, Rep. Prog. Phys. **68**, 1883 (2005).
[52] M. A. Yurkina and A. G. Hoekstra, J. Quant. Spectrosc. Rad. Transf. **106**, 558 (2007).
[53] O. J. F. Martin, C. Girard, and A. Dereux, Phys. Rev. Lett. **74**, 526 (1995).
[54] E. Sassaroli, K. C. P. Li, and B. E. O'Neill, Phys. Med. Biol. **54**, 5541 (2009).
[55] M. I. Tribelsky, A. E. Miroshnichenko, Y. S. Kivshar, and B. S. Luk'yanchuk, Phys. Rev. X **1**, 021024 (2011).
[56] M. Rashidi-Huyeh, S. Volz, and B. Palpant, Phys. Rev. B **78**, 125408 (2008).
[57] J. H. Hodak, A. Henglein, and G. V. Hartland, J. Chem. Phys. **112**, 5942 (2000).
[58] R. R. Letfullin, T. F. George, G. C. Duree, and B. M. Bollinger, Adv. Opt. Technol. **2008**, 251718 (2008).
[59] G. Baffou, M. P. Kreuzer, F. Kulzer, and R. Quidant, Opt. Express **17**, 3291 (2009).
[60] B. Valeur, Molecular Fluorescence: Principles and Applications (Wiley-VCH, Weinheim, 2007).
[61] J. Donner, S. A. Thompson, M. P. Kreuzer, G. Baffou, and R. Quidant, Nano Lett., DOI: 10.1021/nl300389y.
[62] G. Baffou, P. Bon, J. Savatier, J. Polleux, M. Zhu, M. Merlin, H. Rigneault, and S. Monneret, ACS Nano **6**, 2452–2458 (2012).
[63] Y. de Wilde, F. Formanek, R. Carminati, B. Gralak, P. A. Lemoine, K. Joulain, J. P. Mulet, Y. Chen, and J. J. Greffet, Nature **444**, 740 (2006).
[64] F. Marquier, K. Joulain, J. P. Mulet, R. Carminati, and J. J. Greffet, Phys. Rev. B **69**, 155412 (2004).
[65] J. A. Schuller, T. Taubner, and M. Brongersma, Nature Photon. **3**, 658 (2009).
[66] J. M. Stern, J. Stanfield, W. Kabbani, J. T. Hsieh, and J. A. Cadeddu, J. Urol. **179**, 748 (2008).
[67] N. G. Khlebtsov and L. A. Dykman, J. Quant. Spectrosc. Rad. Transf. **111**, 1 (2010).
[68] E. Boisselier and D. Astruc, Chem. Soc. Rev. **38**, 1759 (2009).
[69] R. Brayner, Nano Today **3**(1-2), 48 (2008).
[70] E. E. Connor, J. Mwamuka, A. Gole, C. J. Murphy, and M. D. Wyatt, Small **1**(3), 325 (2005).
[71] X. Huang, P. K. Jain, I. H. El-Sayed, and M. A. El-Sayed, Laser Med. Sci. **23**, 217 (2008).
[72] P. K. Jain, I. H. El-Sayed, and M. A. El-Sayed, Nano Today **2**(1), 18 (2007).
[73] F. X. Gu, R. Karnik, A. Z. Wang, F. Alexis, E. Levy-Nissenbaum, S. Hong, R. S. Langer, and O. C. Farokhzad, Nano Today **2**(3), 14 (2007).
[74] S. Lal, S. E. Clare, and N. J. Halas, Acc. Chem. Res. **41**, 1842 (2008).
[75] P. Cherukuri, E. S. Glazer, and S. A. Curley, Adv. Drug Deliv. Rev. **62**, 339 (2010).
[76] E. C. Day, P. A. Thompson, L. Zhang, N. A. Lewinski, N. Ahmed, R. A. Drezek, S. M. Blaney, and J. L. West, J. Neuro-Oncol. **104**(1), 55 (2011).
[77] A. M. Gobin, M. H. Lee, N. J. Halas, W. D. James, R. A. Drezek, and J. L. West, Nano Lett. **7**(7), 1929 (2007).
[78] C. Loo, A. Lowery, N. Halas, J. West, and R. Drezek, Nano Lett. **5**(4), 709 (2005).
[79] E. B. Dickerson, E. C. Dreaden, X. Huang, I. H. El-Sayed, H. Chu, S. Pushpanketh, J. F. McDonald, and M. A. El-Sayed, Cancer Lett. **269**, 57 (2008).
[80] J. Chen, C. Glaus, R. Laforest, Q. Zhang, M. Yang, M. Gidding, M. J. Welch, and Y. Xia, Small **6**(7), 811 (2010).
[81] S. Mallidi, L. T., J. Tam, P. P. Joshi, A. Karpiouk, K. Sokolov, and S. Emelianov, Nano Lett. **9**(8), 2825 (2009).
[82] J. Nam, N. Won, H. Jin, H. Chung, and S. Kim, J. Am. Chem. Soc. **131**(38), 13639 (2009).
[83] A. Sanchot, G. Baffou, R. Marty, A. Arbouet, R. Quidant, C. Girard, and E. Dujardin, ACS Nano (2012), DOI: 10.1021/nn300470j.
[84] L. R. Hirsch, R. J. Stafford, J. A. Bankson, S. R. Sershen, B. Rivera, R. E. Price, J. D. Hazle, N. J. Halas, and J. L. West, Proc. Natl Acad. Sci. USA **100**(23), 13549 (2003).
[85] D. P. O'Neal, L. R. Hirsch, N. J. Halas, J. D. Payne, and J. L. West, Cancer Lett. **209**, 171 (2004).
[86] C. M. Pitsillides, E. K. Joe, R. R. Anderson, and C. P. Lin, Biophys. J. **84**, 4023 (2003).

[87] A. Vogel, J. Noack, G. Hüttman, and G. Paltauf, Appl. Phys. B **81**, 1015 (2005).
[88] A. Vogel and V. Venugopalan, Chem. Rev. **103**, 577 (2003).
[89] M. W. Berns, J. Aist, J. Edwards, K. Strahs, J. Girton, P. McNeill, J. B. Rattner, M. Kitzes, H. W. M., L. H. Liaw, A. Siemens, M. Koonce, S. Peterson, S. Brenner, J. Burt, R. Walter, P. J. Bryant, D. van Dyk, J. Coulombe, T. Cahill, and G. S. Berns, Science **213**, 505 (1981).
[90] M. Fatih Yanik, H. Cinar, H. N. Cinar, A. D. Chisholm, Y. Jin, and A. Ben-Yakar, Nature **432**, 822 (2004).
[91] Y. Arita, M. L. Torres-Mapa, W. Ming Lee, T. Cizmar, P. Campbell, F. J. Gunn-Moore, and K. Dholakia, Appl. Phys. Lett. **98**, 093702 (2011).
[92] A. Urban, T. Pfeiffer, M. Fedoruk, A. Lutich, and J. Feldmann, ACS Nano **5**(5), 3585 (2011).
[93] G. Han, P. Ghosh, M. De, and V. M. Rotello, NanoBioTechnology **3**, 40 (2007).
[94] P. Ghosh, G. Han, M. De, C. K. Kim, and V. M. Rotello, Adv. Drug Deliv. Rev. **60**, 1307 (2008).
[95] B. T. Timko, T. Dvir, and D. S. Kohane, Adv. Mater. **22**, 4925 (2010).
[96] R. Lévy, U. Shaheen, Y. Cesbron, and V. Sée, Nano Rev. **1**, 4889 (2010).
[97] G. Han, C. C. You, B. J. Kim, R. S. Turingan, N. S. Forbes, C. T. Martin, and V. M. Rotello, Angew. Chem. **118**, 3237 (2006).
[98] P. K. Jain, W. Qian, and M. A. El-Sayed, J. Am. Chem. Soc. **128**(7), 2426 (2006).
[99] S. S. Agasti, A. Chompoosor, C. C. You, P. Ghosh, C. K. Kim, and V. M. Rotello, J. Am. Chem. Soc. **131**, 5728 (2009).
[100] E. Y. Lukianova-Hleb, A. P. Samaniego, J. Wen, L. S. Metelitsa, C. C. Chang, and D. O. Lapotko, J. Control. Release **286**, 293 (2011).
[101] C. C. Chen, Y. P. Lin, and C. W. Wang, J. Am. Chem. Soc. **11**(3709) (128).
[102] A. Wijaya, S. B. Schaffer, I. G. Pallares, and K. Hamad-Schifferli, ACS Nano **3**(1), 80 (2008).
[103] S. E. Lee, G. L. Liu, F. Kim, and P. L. Lee, Nano Lett. **9**(2), 562 (2009).
[104] S. Yamashita, H. Fukushima, Y. Akiyama, Y. Niidome, T. Mori, Y. Katayama, and T. Niidome, Bioorg. Med. Chem. **19**, 2130 (2011).
[105] A. Barhoumi, R. Huschka, R. Bardhan, M. W. Knight, and N. J. Halas, Chem. Phys. Lett. **482**, 171 (2009).
[106] M. S. Yavuz, Y. Cheng, J. Chen, C. M. Cobley, Q. Zhang, M. Rycenga, J. Xie, C. Kim, K. H. Song, A. G. Schwartz, L. V. Wang, and Y. Xia, Nature Mater. **8**, 935 (2009).
[107] L. Paasonen, T. Laaksonen, C. Johans, M. Yliperttula, K. Kontturi, and A. Urtti, J. Control. Release **122**, 86 (2007).
[108] L. J. E. Anderson, E. Hansen, E. Y. Lukianova-Hleb, J. H. Hafner, and D. O. Lapotko, J. Control. Release **144**, 151 (2010).
[109] S. J. Leung, X. M. Kachur, M. C. Bobnick, and M. Romanowski, Adv. Funct. Mater. **21**, 1113 (2011).
[110] H. Takahashi, Y. Niidome, and S. Yamada, Chem. Commun. p. 2247 (2005).
[111] R. Huschka, J. Zuloaga, M. W. Knight, L. V. Brown, P. Nordlander, and N. J. Halas, J. Am. Chem. Soc. **133**(31), 12247 (2011).
[112] D. Boyer, P. Tamarat, A. Maali, B. Lounis, and M. Orrit, Science **297**, 1160 (2002).
[113] M. Selmke, M. Braun, and F. Cichos, ACS Nano (in press, DOI: 10.1021/nn300181h).
[114] L. Cognet, C. Tardin, D. Boyer, D. Choquet, P. Tamarat, and B. Lounis, Proc. Natl Acad. Sci. USA **100**, 11350 (2003).
[115] S. Berciaud, L. Cognet, G. A. Blab, and B. Lounis, Phys. Rev. Lett. **93**, 257402 (2004).
[116] D. Lasne, G. A. Blab, S. Berciaud, M. Heine, L. Groc, D. Choquet, L. Cognet, and B. Lounis, Biophys. J. **91**, 4598 (2006).
[117] D. Lasne, G. A. Blab, F. De Giorgi, F. Ichas, B. Lounis, and L. Cognet, Opt. Express **15**(21), 14184 (2007).
[118] A. Gaiduk, P. V. Ruijgrok, M. Yorulmaz, and M. Orrit, Chem. Sci. **1**, 343 (2010).
[119] A. Gaiduk, M. Yorulmaz, P. V. Ruijgrok, and M. Orrit, Science **330**, 353 (2010).
[120] P. Beard, Interface Focus **1**, 602 (2011).
[121] J. Copland, M. Eghtedari, V. L. Popov, N. Kotov, N. Mamedova, M. Motamedi, and A. Oraevsky, Mol. Imaging Biol. **6**, 341 (2004).
[122] M. Eghtedari, A. Oraevsky, J. Copland, N. Kotov, A. Conjusteau, and M. Motamedi, Nano Lett. **7**(7), 1914 (2007).
[123] Q. Zhang, N. Iwakuma, P. Sharma, B. M. Moudgil, C. Wu, J. McNeill, H. Jiang, and S. R. Grobmyer, Nanotechnology **20**, 395102 (2009).
[124] B. Wang, E. Yantsen, T. Larson, A. B. Karpiouk, S. Sethuraman, J. L. Su, K. Sokolov, and S. Y. Emilianov, Nano Lett. **9**(6), 2212 (2009).
[125] C. Kim, E. C. Cho, J. Chen, K. H. Song, L. Au, C. Favazza, Q. Zhang, C. M. Cobley, F. Gao, Y. Xia, and L. V. Wang, ACS Nano **4**, 4559 (2010).
[126] Y. S. Chen, W. Frey, S. Kim, P. Kruizinga, K. Homan, and S. Y. Emilianov, Nano Lett. **11**(2), 348 (2011).
[127] M. T. Carlson, A. J. Green, and H. H. Richardson, Nano Lett. (in press, DOI: 10.1021/nl2043503).
[128] P. Christopher, H. Xin, and S. Linic, Nature Chem. **3**, 467 (2011).
[129] C. N. Baroud, J. P. Delville, F. Gallaire, and R. Wunenburger, Phys. Rev. E **75**, 046302 (2007).
[130] R. H. Farahi, A. Passian, T. L. Ferrell, and T. Thundar, Opt. Lett. **30**(6), 616 (2005).
[131] G. L. Liu, J. Kim, Y. Lu, and L. P. Pee, Nature Mater. **5**, 27 (2006).
[132] V. Garcés-Chávez, R. Quidant, P. J. Reece, G. Badenes, L. Torner, and K. Dholakia, Phys. Rev. B **73**(8), 085417 (2006).
[133] X. Miao, B. K. Wilson, and L. Y. Lin, Appl. Phys. Lett. **92**, 124108 (2008).
[134] J. Donner, G. Baffou, D. McCloskey, and R. Quidant, ACS Nano **5**, 5457–5462 (2011).
[135] W. A. Challener, C. Peng, A. V. Itagi, D. Karns, W. Peng, Y. Peng, X. M. Yang, X. Zhu, N. J. Gokemeijer, Y. T. Hsia, G. Ju, R. E. Rottmayer, M. A. Seigler, and E. C. Gage, Nature Photon. **3**, 220 (2009).
[136] B. C. Stipe, T. C. Strand, C. C. Poon, H. Balamane, T. D. Boone, J. A. Katine, J. L. Li, V. Rawat, H. Nemoto, A. Hirotsune, O. Hellwig, R. Ruiz, E. Dobisz, D. S. Kercher, N. Robertson, T. R. Albrecht, and B. D. Terris, Nat. Photon. **4**, 484 (2010).
[137] N. Yang, G. Zhang, and B. Li, Appl. Phys. Lett. **93**, 243111 (2008).
[138] L. Wang and B. Li, Phys. Rev. Lett. **101**, 267203 (2008).
[139] M. Först, C. Manzoni, S. Kaiser, Y. Tomioka, Y. Tokura, R. Merlin, and Cavalleri, Nature Phys. **7**, 854 (2011).